

TWO THALAMIC PATHWAYS TO PRIMARY AUDITORY CORTEX

H. L. READ,^{a1*} L. M. MILLER,^{a1} C. E. SCHREINER^a
AND J. A. WINER^b

^aW.M. Keck Center for Integrative Neuroscience, University of California at San Francisco, San Francisco, CA 94143, USA

^bDivision of Neurobiology, Department of Molecular and Cell Biology, University of California at Berkeley, Berkeley, CA 94720-3200, USA

Abstract—Neurons in the center of cat primary auditory cortex (AI) respond to a narrow range of sound frequencies and the preferred frequencies in local neuron clusters are closely aligned in this central narrow bandwidth region (cNB). Response preferences to other input parameters, such as sound intensity and binaural interaction, vary within cNB; however, the source of this variability is unknown. Here we examined whether input to the cNB could arise from multiple, anatomically independent subregions in the ventral nucleus of the medial geniculate body (MGBv). Retrograde tracers injected into cNB labeled discontinuous clusters of neurons in the superior (sMGBv) and inferior (iMGBv) halves of the MGBv. Most labeled neurons were in the sMGBv and their density was greater. iMGBv somata were significantly larger. These findings suggest that cNB projection neurons in superior and iMGBv have distinct anatomic and possibly physiologic organization. © 2008 IBRO. Published by Elsevier Ltd. All rights reserved.

Key words: auditory cortex, medial geniculate body, thalamus, parallel pathways.

The auditory thalamus is an obligatory station in the pathway from peripheral receptors to auditory cortex (Winer et al., 2005). The ventral division of the medial geniculate body (MGBv) is the source of >75% of ascending sensory input to the primary auditory cortex (AI) (Middlebrooks and Zook, 1983; Morel et al., 1987; Lee and Winer, 2005). Best frequency (BF) and frequency bandwidth properties are organized topographically in the three dimensions of the MGBv (Rouiller and de Ribaupierre, 1985). MGBv neurons

in turn project to AI, where these features are represented in layer III and layer IV (Read et al., 2002), forming a two-dimensional projection plane (Huang and Winer, 2000; Smith and Populin, 2001).

Previous studies in cat and rabbit found a single low-to-high BF organization or tonotopy in MGBv (Aitkin and Webster, 1972; Imig and Morel, 1985; Brandner and Redies, 1990; Cetas et al., 2002, 2003). Neurons with similar BFs form isofrequency laminae which extend ~3 mm in the dorsal–ventral dimension of MGBv in both species and which correspond anatomically to fibrodendritic laminae (Morest, 1965). The BFs of neighboring laminae differ by as little as 1/4 octave in the cat (Imig and Morel, 1985) or up to one octave in rabbit (Cetas et al., 2001, 2002) MGBv. Reconstruction of physiological recording tracks in cat MGBv (Imig and Morel, 1985) suggests two distinct regions within the laminar subdivision, one with a fine and the other with a coarser tonotopic frequency resolution (Escabi and Read, 2005). Other physiologic studies have suggested that the axis of the spatial frequency gradient changes between the dorsal and ventral parts of the MGBv (Calford and Webster, 1981; Imig and Morel, 1985). These preliminary data led us to suspect distinct anatomical and functional subregions within MGBv, though it is classically considered a single nucleus (Morest, 1965) with lateral (low-to-middle frequency, pars lateralis) and medial (middle-to-high frequency, pars ovoidea) subregions (Imig and Morel, 1985). Hypothesizing that input to central AI may arise from multiple, morphologically distinct populations and areal regions of MGBv, we injected retrograde tracer into AI and examined the MGB projection sources. Since the functional organization of AI is non-homogeneous and can vary substantially between individuals (Schreiner et al., 2000; Read et al., 2001), we chose to inject a reliably identifiable functional subregion, the central narrow bandwidth region (cNB). This region lies near the center of the dorsal–ventral extent of AI and has two salient features: all single cells are narrowly tuned for frequency, and the BF's of the neurons in local clusters are in close register (Schreiner and Sutter, 1992), implying that multi-unit responses are also narrowly tuned.

EXPERIMENTAL PROCEDURES

Surgery, recording, and tracer deposits

Retrograde tracers were injected into the physiologically identified and mapped cNB region in AI of four cats for a total of five injections (one experiment received two deposits). Cortical physiologic and anatomic data from three animals included here have been reported previously (Read et al., 2001). Single- and multiunit responses to a five-octave range of pure tone stimuli were re-

¹ Present address: Division of Behavioral Neuroscience, Psychology, University of Connecticut, Storrs, CT 06269, USA (H. L. Read); Section of Neurobiology, Physiology and Behavior, Center for Mind and Brain, University of California at Davis, Davis, CA 95616, USA (L. M. Miller).

*Correspondence to: H. L. Read, Division of Behavioral Neuroscience, Psychology, University of Connecticut, Storrs, CT 06269, USA. Tel: +1-860-486-4895; fax: +1-860-377-7987.

E-mail address: heather.read@uconn.edu (H. L. Read).

Abbreviations: AI, primary auditory cortex; ANOVA, analysis of variance; BF, best frequency; cNB, central narrow bandwidth; CT β , cholera toxin β subunit; CT β G, cholera toxin β subunit conjugated to gold particles; CV, coefficient of variation; dNB1, first dorsal narrow bandwidth region; iMGBv, inferior part of the ventral division of the medial geniculate body; LGB, lateral geniculate body; MGB, medial geniculate body; MGBv, medial geniculate body, ventral division; sMGBv, superior part of the ventral division of the medial geniculate body; WAHG, wheat-germ agglutinin apo-horseradish peroxidase conjugated to colloidal gold.

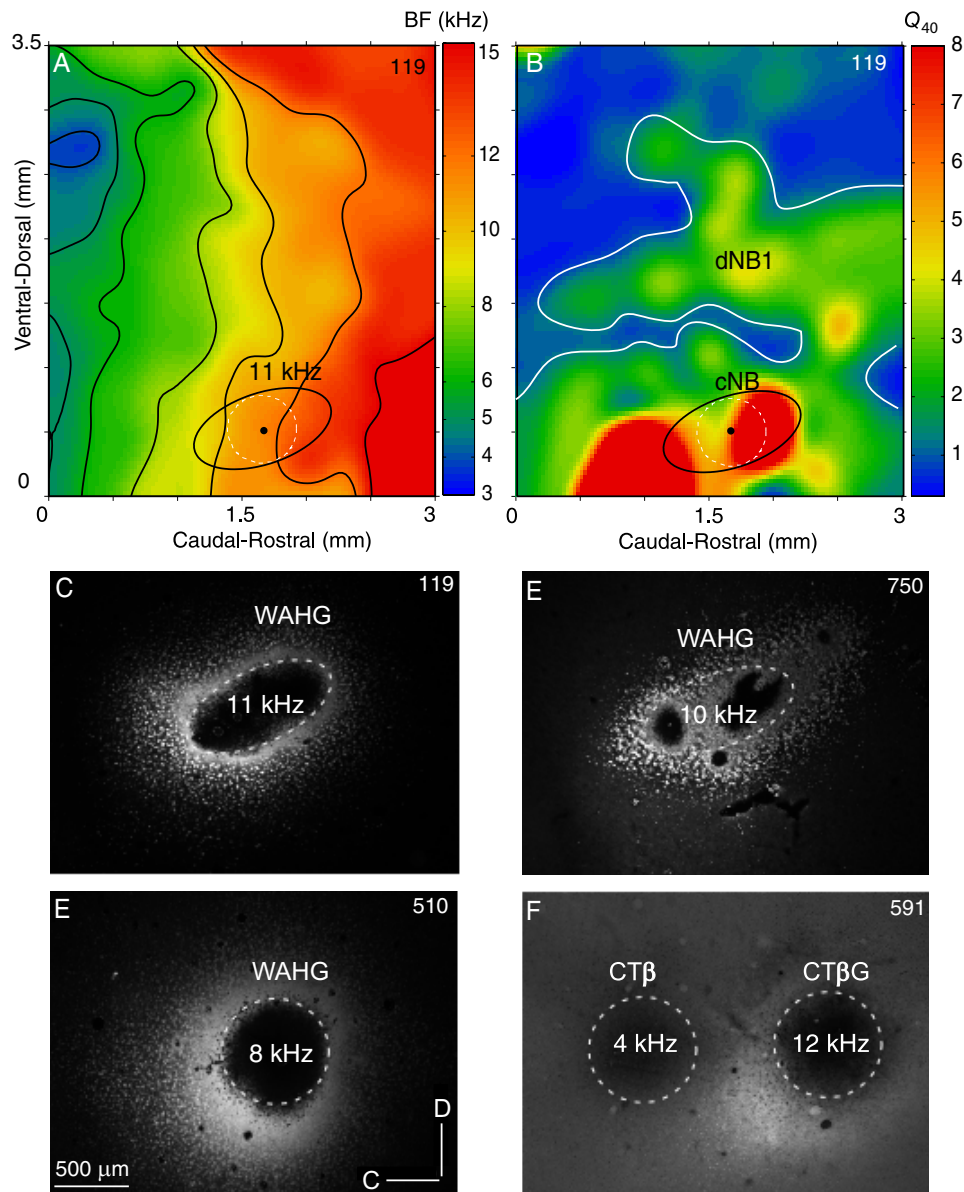


Fig. 1. Frequency representation in AI and injection of a retrograde tracer into the cNB region. Interpolated maps of BF (at threshold) and Q_{40} values are shown for a 3×3.5 mm area of cortex for case 119. BF contours (black lines) are superimposed at $1/3$ octave intervals. Black dot, injection center. Black circle, halo of labeled neurons surrounding the deposit. (A) Retrograde tracer (WAHG) was injected into the 11 kHz representation in AI. The deposit (A, B, black oval) spanned $500 \mu\text{m}$ in the dorso-ventral dimension and $\sim 1000 \mu\text{m}$ across the antero-posterior axis. (B) The tracer deposit was associated with Q_{40} values > 2 (green–red regions). Thalamic labeling appears in Figs. 2 and 3. Broad bandwidth regions (blue) flanked the cNB region and a second peak associated with a dorsal narrow bandwidth region (dNB) was identified with autocorrelation analysis (Read et al., 2001). White lines represent an iso-bandwidth contour of $Q_{40}=1$. (C–E) Darkfield illumination shows WAHG deposits in the cNB region of AI for three right hemispheres from three experiments (119, 510, 750). (F) Combined bright- and darkfield illumination shows CT β and CT β G deposits in the cNB region of AI in the same right hemisphere of a fourth experiment (591). (C–F) The frequency labels (kHz) indicate the BF recorded at the corresponding center of the injection. Physiologic and cortical anatomic data for cases 119, 510, 750 have appeared elsewhere (Read et al., 2001).

corded in layers IIIb and IV of AI in ketamine-anesthetized adults. Sound pressure level and pure tone frequency were pseudorandomly varied and presented binaurally to determine frequency tuning parameters, including BF at threshold, normalized tuning-curve bandwidth ($Q_{40} = \text{BF}/\text{bandwidth } 40 \text{ dB above threshold}$) and, in some cases, binaural interaction properties. Upper and lower limits for calculating bandwidth and Q_{40} were constrained by a five-octave window centered around the BF at threshold. Parallel recording tracks were separated by $100\text{--}300 \mu\text{m}$ (average:

$\sim 150 \mu\text{m}$). Track positions were mapped in reference to the surface vasculature and covered an area of $\sim 3 \times 3 \text{ mm}^2$. In the first 34 h of mapping, the cNB and surrounding broad-bandwidth regions were located (e.g. Fig. 1B). BFs and Q values for each recording site were plotted and tessellated prior to interpolating. An average mapped cNB region spanned $\sim 1.3 \text{ mm}$ in the dorsal–ventral extent of injected isofrequency contours between 4 and 12 kHz. The location and size of bandwidth regions for three of the five injection cases have been quantified with autocorrelograms

(Read et al., 2001). A similar bandwidth organization was found in the fourth hemisphere included here. A dorsal, narrow bandwidth (dNB1) region lying superior to cNB created a second peak in the spatial autocorrelation functions for three of the four mapped areas analyzed. Variations in the map extent between cases reflect experimental limitations such as blood vessels and time available for mapping. All three standard binaural types were found in the cNB region (contralateral stimulation was usually excitatory and ipsilateral was excitatory, inhibitory or non-effective). Summaries of the Q_{40} map, autocorrelograms and injection site location for three of the four cases analyzed here are available (Read et al., 2001).

Tracers and histology

Cats were anesthetized with ketamine HCl (10 mg/kg) and acepromazine (0.28 mg/kg, i.m.). An i.v. line was installed and dexamethasone (0.14 mg/kg, i.v.) and atropine (0.04 mg/kg/day, s.c.) were infused and supplemented every 12 h to prevent brain swelling and fluid accumulation. Surgical anesthesia was induced with sodium pentobarbital (30 mg/kg) and maintained throughout the surgical procedures, which included a tracheotomy to facilitate respiration and reduce respiratory noise and a craniotomy to expose temporal cortex. After surgery, an areflexive state was maintained with continuous infusion of ketamine (2–4 mg/kg/h) and diazepam (0.4–1 mg/kg/h) in 3% dextrose lactated Ringer's solution. Heart and respiratory rate, and body temperature and reflexes were monitored and infusion rates were adjusted accordingly.

Several measures were taken to generate robust labeling in MGBv and to prevent significant tracer diffusion beyond the cNB. A retrograde tracer was injected in cNB with a volume displacement nanoliter injector (Drummond Scientific Company, Broomall, PA) at three to four cortical depths spanning 800–1200 μm with a total of 30–80 nL in a track. Injection pipettes were oriented $\sim 15^\circ$ to the pia at the same angle as the recording electrode. A small spread in the tracer deposit can occur by capillary action. Due to the penetration angle, the anterior–posterior spread of the tracer along the pipette track was slightly elongated in two of the deposits compared with the dorsal–ventral spread (e.g. Fig. 1, black oval). Retrograde tracers were wheat-germ agglutinin apo-horse-radish peroxidase conjugated to colloidal gold (WAHG) (Basbaum and Menetrey, 1987), cholera toxin β subunit (CT β), and cholera toxin β subunit conjugated to gold particles (CT β G, List Biological Laboratories, Campbell, CA) (Luppi et al., 1990). Single WAHG injections were made in physiologically mapped right hemispheres of three cats (Fig. 1C–E); in a fourth cat, CT β and CT β G injections matched in size were made ~ 1.5 mm apart (Fig. 1F). Survivals were 3.5 (± 1) days. We find that these three tracers are indistinguishable in quality and rate of labeling (Lee et al., 2004) and the areal labeling and density differences in MGBv were similar for all five injections (see Results). At experiment's end, the animal was given a lethal dose of sodium pentobarbital (>50 mg/kg) and perfused transcardially with 4% paraformaldehyde. The cortex was removed and flattened and the diencephalon was blocked stereotaxically in the skull in the coronal plane and both were equilibrated in 30% sucrose solution and then frozen-sectioned at 40 μm . The cortex was sectioned tangential to the flattened surface. A fiducial mark in the thalamus outside the medial geniculate body (MGB) extended the length of the thalamus. Every sixth section was Nissl-stained with Cresyl Violet to delineate thalamic nuclei and the other sections were reacted for one or both tracers. Architectonic subdivisions were drawn independently of the pattern of retrograde labeling. Nissl-stained sections were used to determine medial and ventral divisions of the MGB as well as other thalamic nuclei corresponding to subdivision used in prior cytoarchitectonic studies (Morest, 1965). Anatomic features used to delineate borders included: laminar pattern, somatic cell size, and orientation. There was close accord between our nuclear borders and the scheme of subdivisions based on recording stud-

ies (Aitkin and Webster, 1972; Imig and Morel, 1985), and patterns of connectivity with the inferior colliculus (Calford and Aitkin, 1983) and auditory cortex (Winer et al., 1977), and with prior views of MGB divisions from morphological and connective studies (Middlebrooks and Zook, 1983; Winer, 1985). Nuclear borders also were in close accord with those in previous work (Huang and Winer, 2000) and the subdivisions in standard references (Ber-man and Jones, 1982).

Data analysis

Histological processing methods used here appear elsewhere (Read et al., 2001). WAHG (Basbaum and Menetrey, 1987) or CT β G labeling was intensified with silver for light microscopy. CT β was visualized with appropriate primary (List Biological Laboratories, Campbell, CA) and secondary antibodies (Vector Laboratories, Burlingame, CA) and intensified with diaminobenzidine. The locus of labeled neurons was manually plotted with a light microscope equipped with a motorized stage, Lucivid monitor, and Neurolucida software package (MicroBrightField, Colchester, VT, USA). Neuron cell bodies were plotted using 40–60 \times objectives. Adjacent sections stained for Nissl substance and retrogradely labeled sections were traced anatomically and aligned via vascular landmarks. Cell sizes were scored by a colleague (N.H.) unaware of the purpose of this analysis. The labeled cells were plotted and the size of their somata was measured for data from five tracer deposits. Measurements were made by marking the estimated center of a soma that included a nucleus, then scoring somatic boundaries and junctures between the soma and the first proximal processes at 10 positions using the Nucleator software (MicroBrightField) and a 60 \times oil immersion objective. Somata with labeling that obscured the nucleus were classified as neuronal if they had three or more processes extending from the soma. Cell positions, numbers and sizes were analyzed from non-contiguous histological sections to avoid counting the same cell in multiple sections. A circle with the average radius from the soma center estimated the soma size (using Matlab and MicroBrightField software). Sections with labeled neurons were aligned using the midline and blood vessels as reference points. Somatic sizes and locations were analyzed in a 3 \times 3 mm 2 area that was divided into six 500 \times 3000 μm bins. The most inferior bin in MGBv corresponded to pars lateralis in Nissl-stained adjacent sections. The next two bins (1000 and 1500 μm) had labeling within both pars ovoidea and pars lateralis. The most superior three bins (2000, 2500 and 3000 μm) were in the pars lateralis. Multivariate analysis of variance (ANOVA) tested for mean size differences, two-way ANOVA for differences between pairs of spatial bins. For all comparisons the χ^2 test for distribution differences were significant if the two-way ANOVA was significant; therefore only the ANOVA statistics are reported.

Two dimensional density histograms were made from cell position-plots to quantify and compare labeling topography, spread and density (Read et al., 2001). Density histograms (100 \times 100 μm^2 bin widths) spanned 4 \times 4 mm 2 in the coronal plane and included sections with maximal number of labeled cells. Data from four sequential sections separated by 120 μm and covering 480 μm in caudal–rostral dimension were aligned and summed to quantify cell density; thus, labeling from five experiments and 20 sections was used for this analysis. Peaks in cell density were deemed significant if they were two or more standard deviations above the mean ($P < 0.001$; bootstrapped histogram with 250 random samples). The coefficient of variation (CV, the standard deviation divided by the mean, $CV = \sigma / \bar{x}$ and $\sigma = \sqrt{\sum (x - \bar{x})^2 / n - 1}$) for the resulting density histograms was calculated and plotted for each 100 μm bin. A value of 0.0001 was substituted for bins with a mean value of zero. The CV analysis is a convenient way to locate significant peaks in the two-dimensional density histograms and to demonstrate continuous or discontinuous patterns of labeling.

RESULTS

Mapping AI frequency and bandwidth tuning

Retrograde tracers were injected into the mid-frequency cNB region of AI in four cats for a total of five injections. BFs and bandwidths of layer III–IV neurons were topographically organized along approximately orthogonal axes in AI (Fig. 1). High-resolution mapping revealed a low-to-high frequency gradient (Fig. 1A), containing a dominant cNB region (Q_{40} values >3) flanked dorsally and ventrally by sites with predominantly broad bandwidth (Fig. 1B) neurons (Q_{40} values <2 ; blue regions). Neurons with very narrow bandwidth (Q_{40} values >3) were also found in the first dNB1 region (Read et al., 2001). Deposit sites were $<700 \mu\text{m}$ long in their maximal dorso-ventral extent and, thus, were confined to the $\sim 1.3 \text{ mm}$ -wide cNB region (Fig. 1C–F). In one case, CT β and CT β G were injected in the cNB region at 4 and 12 kHz, respectively; their injection perimeters did not overlap (Fig. 1F).

Patterns of labeling identify subregions within the MGB

The size of retrogradely labeled somata was related to their dorso-ventral MGBv position. The distribution of retrograde thalamic labeling crossed much of the superior-to-inferior MGBv axis (Fig. 2). In cat 119, the injection was within the cNB region of the 11 kHz isofrequency contour (Fig. 1A, B). The labeling was confined to the MGB as determined in adjacent Nissl preparations (e.g. as drawn in Fig. 3A). Higher magnification (40 \times) images showed qualitative differences in cell size and packing density for superior (Fig. 2B) vs. inferior (Fig. 2C) MGBv neurons. Labeled cells in the inferior part of the ventral division of the medial geniculate body (iMGBv) had larger somata with more highly branched and radiate dendritic arbors. These large MGBv cells resembled tufted spindle-shaped and wide field cells in the cat (Morest, 1964, 1965) and rat (Winer et al., 1999) MGBv. Dendrites of iMGBv neurons were labeled more extensively. Labeling was cytoplasmic and extended to the border of the nuclear membrane; heavily labeled somata were present in both regions (compare Fig. 2B and 2C).

We excluded the possibility that these large neurons were located outside the boundaries of MGBv (see Experimental Procedures) since the medial division of the MGB contains larger neurons with a more heterogeneous morphology (Winer and Morest, 1983a). Typical regional labeling pattern and architectonic boundaries in two experiments (experiments 119, 510; Fig. 3A, B) show that most labeled cells lay within the classically defined MGBv pars lateralis and ovoidea (Morest, 1964, 1965). The areal labeling pattern was similar in neighboring sections. In this example, four sections near the region of maximal labeling span $720 \mu\text{m}$ in the rostral–caudal dimension (Fig. 3C–F). These sections are separated by $240 \mu\text{m}$ gaps. A few labeled cells were noted in the MGBv rostral pole (not shown).

Two populations of MGBv neurons project to AI

Cross-sectional areas of labeled neurons were larger in the inferior half of the MGBv. Plots were made at systematic intervals along the rostral–caudal MGB axis. Soma sizes were measured in one to four $40 \mu\text{m}$ thick sections per experiment. The pattern of retrograde labeling was similar in all sections, making a larger sample unnecessary. Somatic areas were plotted (Fig. 3) and assigned to one of six $500 \times 3000 \mu\text{m}^2$ (medial–lateral by superior–inferior axes, respectively) bins for statistical analysis (Fig. 3C–F). Cell somatic size differed significantly along the dorsal–ventral axis but not in the rostral–caudal axis in four sections from one experiment (cat 119; $F=22.47$, $df=5$, $P<0.002$; Fig. 3C–F). Similarly somatic size differed significantly along the dorsal–ventral axis for data from all five experiments ($F=32.93$, $df=5$, $P<0.002$, 4B). Soma size in the inferior three bins was significantly larger than in the superior three bins ($F=4.07$, $df=20$, $P<0.002$). A statistical interaction (Bin \times Section) was seen across the five experiments, likely reflecting differences in tracer deposit size, transport time and bin locus variations across experiments. The mean cell size in the most inferior $500 \mu\text{m}$ bin (bin 1) differed from that of the two most superior bins ($df=4$; $F=(13-31)$; $P<0.002$; Fig. 4A, C). Larger mean somatic areas were seen in inferior bins even when the somata were in pars lateralis (Fig. 3C–F). A similar difference was seen when comparing bins 2 and 3 with the three superior bins (Fig. 4B: asterisks). Mean somatic areas in the inferior three bins were larger and not significantly different from each other (Fig. 4B, large filled gray circles; 500 , 1000 , and $1500 \mu\text{m}$ bins; mean \pm S.D.: $369 \pm 116 \mu\text{m}^2$, $354 \pm 137 \mu\text{m}^2$ and $295 \pm 85 \mu\text{m}^2$, respectively). Somata in the three superior bins were $\sim 25\%$ smaller ($260 \pm 102 \mu\text{m}^2$, $255 \pm 85 \mu\text{m}^2$, and $245 \pm 88 \mu\text{m}^2$, respectively). Since the cytoplasmic filling was neither differential nor incomplete, we conclude that the documented somatic size differences are valid. Thus, mean cross-sectional area varied as a function of superior–inferior MGBv position and was significantly larger in the inferior 0-to- $1500 \mu\text{m}$ of MGBv, suggesting a dorsoventral MGBv gradient of somatic size.

Areal patterns of thalamocortical projections

The total number of labeled cells was larger in superior than iMGBv. The superior and inferior 1.5 mm of MGBv contained 57% and 43% of the total number of retrogradely-labeled neurons, respectively. In addition, the packing density of AI (cNB) projection neurons/ $100 \mu\text{m}^2$ was twice as large in the superior part of the ventral division of the medial geniculate body (sMGBv). Cell density measures in $100 \times 100 \mu\text{m}^2$ bins in sMGBv showed that the bin with the maximal mean density contained 12–20 neurons (red), while the highest density in the inferior part of MGBv was only six neurons/bin (Fig. 5). Thus, peak-labeling density was two times greater in sMGBv. In spite of differences in cell density or dispersion, there was a topographic frequency gradient for labeling; however, the higher dispersion and lower density suggests more frequency contour overlap in the inferior part of the ventral division of the

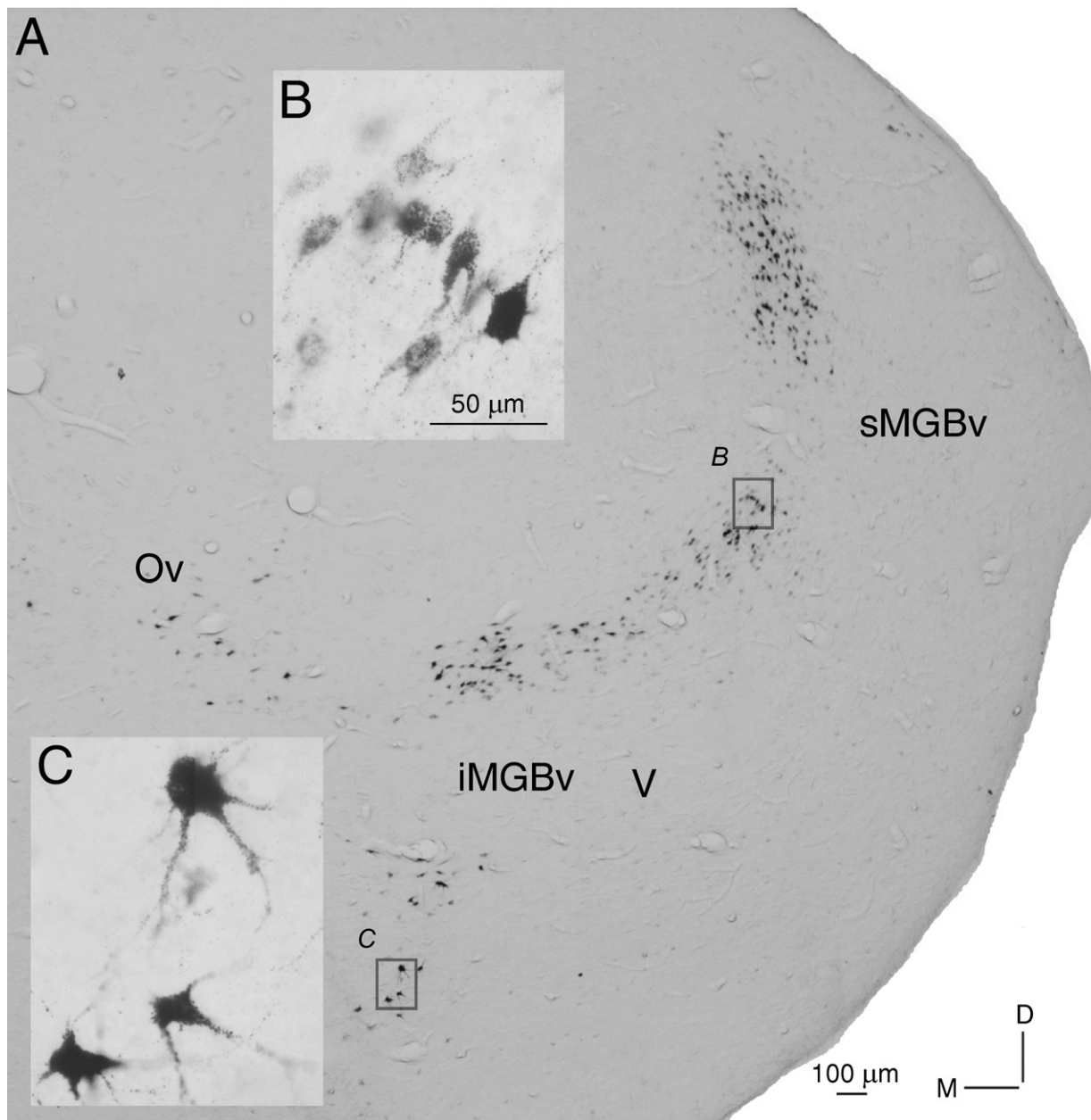


Fig. 2. Photomicrograph of retrogradely labeled MGB neurons after a WAHG injection into the 11 kHz frequency contour and cNB region in case 119. (A) Patches of retrogradely-labeled neurons extend through most of the superior–inferior MGBv axis. Insets: higher magnification views of labeled neurons in this section in sMGBv (B) and iMGBv (C). Note that iMGBv includes neurons that are from the pars ovoidea (Ov). Many iMGBv neurons are larger and more stellate whereas the superior neurons are classic bushy tufted principal cells. A planapochromatic lens and appropriate illumination optimized contrast. Confirmation that labeling was intracellular was documented at higher magnification.

medial geniculate body (iMGBv) (Fig. 4D). Labeled cells along the isofrequency domain were not uniformly distributed but showed regions of high or low cell density. Local peaks in labeling density occur in both the sMGBv and iMGBv. The variation in labeling density was examined to search for significant local MGBv maxima. The variation in labeling density was lowest in the sMGBv (maximum $\pm 160 \mu\text{m}$; $\text{CV} < 0.3$) and highest in iMGBv (maximum $\pm 160 \mu\text{m}$; $\text{CV}: 0.4\text{--}0.9$) (Fig. 5). A superimposed contour (black) denotes the limits of labeling with low CV

values. Thus, while MGBv labeling appears homogeneous and widespread in photomicrographs (Fig. 2) and scatter plots (Figs. 3, 5D) it is inhomogeneous within isofrequency laminae with maximal density in the superior 1.5 mm of MGBv.

DISCUSSION

We found that, contrary to previous suggestions, input from the principal thalamic nucleus, MGBv, to the AI cNB

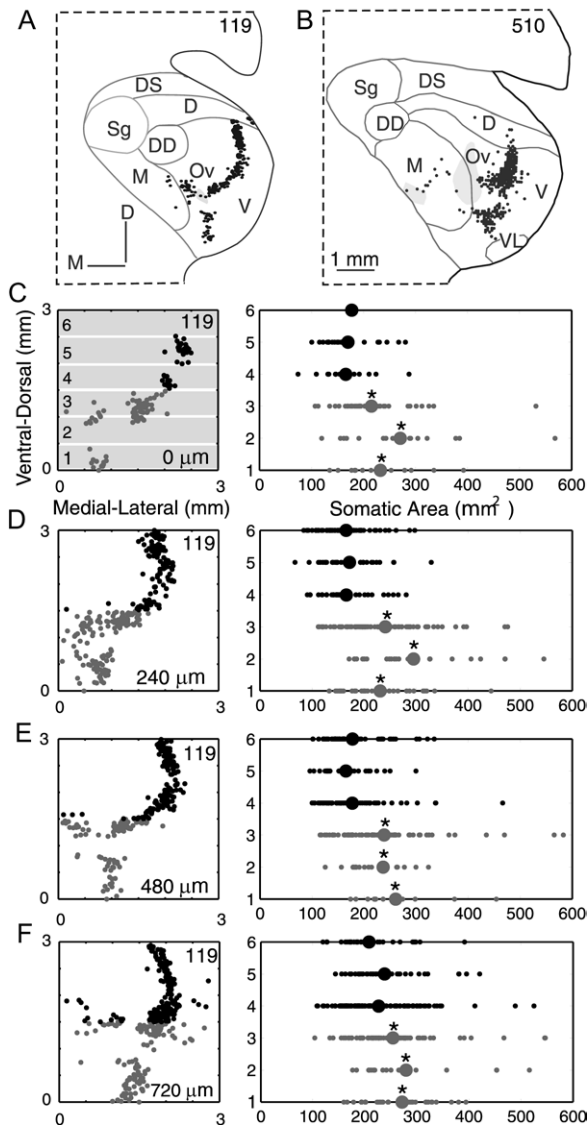


Fig. 3. Mean size of labeled somata is smaller in superior versus inferior halves of MGBv in all sections from a single tracer experiment. (A, B) Plots of retrogradely labeled neurons were superimposed on Nissl tracings of thalamic nuclei in the sections with the greatest labeling. Some discontinuities in labeling coincided with the brachium of inferior colliculus (gray area) in these sections. (C–F) (Left column) Positions of labeled MGBv somata in a non-contiguous series of sections separated rostro-caudally by $240\ \mu\text{m}$, across $720\ \mu\text{m}$. Mean somatic size was computed for each of the $500 \times 3000\ \mu\text{m}^2$ bins (gray; numbered 1–6) in (C). Black dots, cell positions in bins with a smaller mean soma size (right side) than cells in bins 1–3 (i.e. sMGB). Gray dots, cells with a larger mean size (i.e. iMGB) than those in bins 4–6 (i.e. iMGB). (Right column) Somatic areas of cells from the left column. Somatic diameters, small solid dots; means, large dots. Asterisk, inferior bins with somatic means significantly larger ($P < 0.002$) than those of the soma distributions in the three superior bins (ANOVA).

region is not homogenous with respect to the dorso-ventral axis of the MGBv. The major input to the AI cNB region came from the sMGBv. Further, sMGBv and iMGBv projection neurons had different somatic size distributions, packing density patterns, and density peak locations (Figs. 2–5). Both sMGBv and iMGBv cells were organized into

frequency lamina (Fig. 5D); however, iMGBv projections were more diffuse with more distance between neighboring neurons (Fig. 5).

Previous physiologic recordings in MGBv hinted at a dorso-ventral reversal in frequency organization when traversing pars lateralis and pars ovoidea (Calford and Webster, 1981; Imig and Morel, 1985). The shape of the labeled regions in our study supports this and more specifically suggests that the locus for a shift in the frequency gradient occurs near the border of the superior and iMGBv including the pars lateralis (Fig. 5D). Our data also suggest a coarser tonotopic iMGBv organization (Fig. 5D) as suggested previously (Calford and Webster, 1981; Imig and Morel, 1985; Morel and Imig, 1987). This frequency gradient change in the dorso-ventral axis of MGBv could serve as a landmark for sMGBv and iMGBv in future physiologic studies.

This study elaborates on the functional organization of thalamocortical input to AI, demonstrating several anatomic distinctions between thalamic projection neurons in dorsal and ventral halves of MGBv. The dorso-ventral and rostral–caudal extent of the present labeling corresponds to that described previously (Andersen et al., 1980; Middlebrooks and Zook, 1983; Rodrigues-Dageaff et al., 1989). Other studies found that input from MGBv to central AI was highly convergent, arising from over 3 mm in the MGBv dorso-ventral axis (Middlebrooks and Zook, 1983; Morel and Imig, 1987; Stanton and Harrison, 2000). These prior reports may have given the impression that the convergent input from superior and inferior parts of MGBv was similar. However, spatial variation in cell density, the distinct local maxima in labeling, and the soma size distributions are not evident in photomicrographs or scatter plots of cell positions in this or the prior studies. Thus, the present study extended previous descriptions of thalamic input to central AI by demonstrating that convergent MGBv input arises from regions of MGBv with distinct patterns of labeling density. It is possible that sMGBv and iMGBv are a continuous functional gradient for frequency and other response features, but the present study finds that they are anatomically non-homogeneous in several respects including cell density.

This study raises the possibility that sMGBv and iMGBv may be functional and anatomic subdivisions within the MGB. Dorsal, medial and ventral cytoarchitectonic divisions of MGB, based on soma size, morphology and laminar organization (Morest, 1965; Winer and Morest, 1983a,b) have been confirmed by functional studies (Calford, 1983; Calford and Aitkin, 1983; Bordin and LeDoux, 1994). The largest somata within our sample of iMGBv were still far smaller (Fig. 4B; $700\ \mu\text{m}^2$) than magnocellular somatic sizes ($1400\ \mu\text{m}^2$) reported for the medial division of MGB in cat (Morest, 1965; Winer and Morest, 1983a,b). However, we find a significant somatic size difference for sMGBv and iMGBv as well (Fig. 2). A different type of anatomic approach would be needed to fully characterize the dendritic morphology differences suggested in the present study for iMGBv and sMGBv neurons. We discount the possibility that the large cells with radiate dendrites we find in iMGBv were simply more heavily labeled

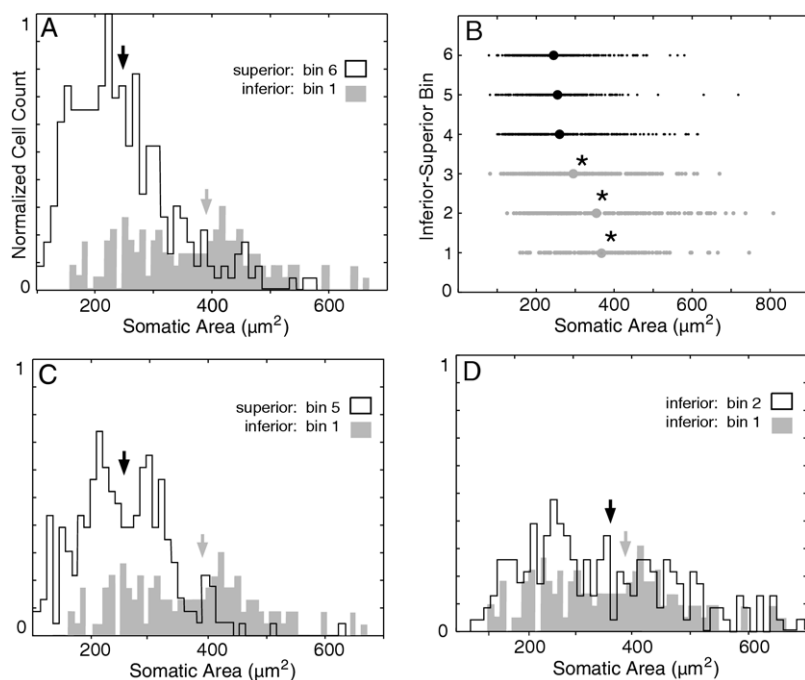


Fig. 4. Average somatic size of labeled neurons is larger in the iMGBv in five injections. (A, C, D) Histograms of somatic areas. Gray-filled histograms, somatic areas for the inferior 500 μm bin. Black histograms, somatic areas in bins 6 (A), 5 (C), and 2 (D), corresponding to 3000, 2500, and 1000 μm intervals, respectively. Somatic sizes were measured and positions plotted as described in Fig. 3. Arrows, means. (B) Somatic areas for all bins. Large dot, mean somatic area. Asterisk, inferior bins (gray) with significantly larger means ($P < 0.002$; see Experimental Procedures for statistical analysis) than any of the somatic size distributions in the superior bins 4–6 (black).

versions of the same sorts of cells within sMGBv since there were equally heavily labeled neurons in sMGBv (Fig.

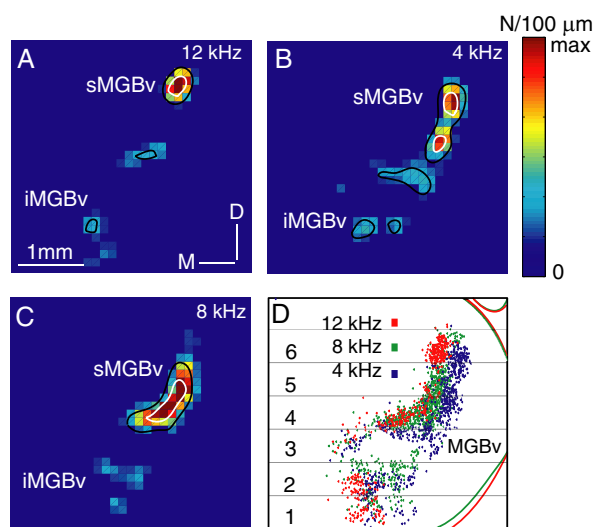


Fig. 5. The density of retrogradely-labeled neurons differs between sMGBv and iMGBv. (A–C) Rainbow spectrum indicates density (blue/low to red/high). Black and white superimposed contours are 25% and 67% of maximum labeling density, respectively. (D) Superimposition of the three cell position plots used to construct density histograms (A–C). Blue, green, and red dots correspond to somatic positions in density histograms in A, B, and C, respectively. The corresponding injection site BFs for A, B, and C appear in Fig. 2B (12 kHz), 2B (4 kHz) and 2C (8 kHz), respectively. Color bar (red), maximal density of 12, 15, and 16 neurons/100 μm for A, B, and C, respectively.

2, inset B) and these appeared to have morphologies distinct from the more common sMGBv principal neurons (Fig. 2, inset B). Notwithstanding technical limitations, we found that iMGBv somatic sizes were $\sim 25\%$ larger than those in sMGBv (Fig. 4B). Such cell size differences for iMGBv and sMGBv resemble those observed for functionally distinct A- and C-laminae in cat lateral geniculate body (LGB) (Guillery, 1966). Functionally distinct LGB laminae are segregated spatially by fibers that separate the A- and C-subregions into independent laminae. Likewise, the brachium of the inferior colliculus sometimes divides sMGBv and iMGBv (Fig. 3A, B); even when the brachium did not separate them, CV analysis revealed significantly different peaks of labeling in sMGBv and iMGBv (Fig. 5, contours). Hence, the two regions of MGBv differed in soma size, soma density per unit area of MGBv, and in the location of density peaks and laminar profiles.

The sMGBv and iMGBv subregions described here do not simply rename divisions we and others have defined as the pars ovoidea and pars lateralis. MGBv has been anatomically and functionally subdivided into pars lateralis and pars ovoidea (Morest, 1965; Calford, 1983; Imig and Morel, 1985). However, the sMGBv and iMGBv in the present study were fully or predominantly within pars lateralis based on examination of neighboring Nissl sections. Had the data been grouped into pars lateralis versus pars ovoidea and compared within that framework, we would not have found the same trend, as some of the largest cells and some of the smallest cells were within the pars lateralis of the MGBv. Therefore, the present inferior–superior

distinction reflects statistical differences in somatic size, cell density, and differential connectivity in the dorso-ventral MGBv axis and not on previously defined Nissl based compartmentalization within MGBv.

Possible physiologic correlates of the two lemniscal thalamocortical pathways

Examination of MGB input to the cNB region in AI was motivated by the observation that layer III cNB neurons project primarily to a dorsal NB region of AI and avoid the ventral and dorsal broad bandwidth regions (Read et al., 2001). Thus, the cNB and dNB1 regions of AI (Fig. 1, cNB and dNB1, green/red) contribute to a cortical network with sound processing capabilities distinct from the broad bandwidth regions (Fig. 1, blue). The cNB region occupies ~1300 μm in the dorsal–ventral axis and includes a heterogeneous population of cells with other response properties, such as binaural interaction types. The present study suggests that heterogeneity of cNB response properties may stem from heterogeneity in their MGBv projections.

The convergence of sMGBv and iMGBv pathways in the cNB region could account for two of the principal spectral receptive field transformations in AI. These spectral profiles are seen when synaptically connected MGBv and AI neurons were recorded simultaneously (Miller et al., 2001). In one class of thalamocortical pairs, cortical spectral receptive field properties were so similar to their MGBv partner that these properties were regarded as essentially “inherited.” In another class, MGBv and AI neuron spectral receptive fields overlapped, but their BF centers were shifted by up to $\pm 1/4$ octave corresponding to a total possible thalamic convergence of $1/2$ octave. In such cases, the AI receptive field was “constructed” from convergence of multiple BF sources in MGBv (Miller et al., 2001). AI spectral properties might be “inherited” by a cNB region that receives the bulk of its projections from the sMGBv. Conversely, a higher degree of spectral convergence could arise from the tonotopically more coarse iMGBv. Thus, the thalamocortical receptive field transformations observed previously may embody differences in thalamic projection neurons and their specific targets in AI.

Acknowledgments—Research was supported by National Institutes of Health grant numbers: R01DC 02260 (C.E.S.) and R01DC 02319 (J.A.W.). We thank D. T. Larue and D. R. Nauen for histological and technical assistance, and we are grateful to N. Higgins, Dr. B. H. Bonham and Dr. M. E. Escabi for contributions to recording and analysis. We acknowledge our colleagues at the Keck Center for advice and helpful discussions. We thank Dr. D. L. Oliver for access to microscopes and software.

REFERENCES

- Aitkin LM, Webster WR (1972) Medial geniculate body of the cat: organization and responses to tonal stimuli of neurons in ventral division. *J Neurophysiol* 35:365–380.
- Andersen RA, Knight PL, Merzenich MM (1980) The thalamocortical and corticothalamic connections of AI, AII, and the anterior auditory field (AAF) in the cat: evidence for two largely segregated systems of connections. *J Comp Neurol* 194:663–701.
- Basbaum AI, Menetrey D (1987) Wheat germ agglutinin-apoHRP gold: a new retrograde tracer for light- and electron-microscopic single- and double-label studies. *J Comp Neurol* 261:306–318.
- Berman AL, Jones EG (1982) The thalamus and basal telencephalon of the cat: a cytoarchitectonic atlas with stereotaxic coordinates. Madison: University of Wisconsin Press.
- Bordi F, LeDoux JE (1994) Response properties of single units in areas of rat auditory thalamus that project to the amygdala. I. Acoustic discharge patterns and frequency receptive fields. *Exp Brain Res* 98:261–274.
- Brandner S, Redies H (1990) The projection of the medial geniculate body to field AI: organization in the isofrequency dimension. *J Neurosci* 10:50–61.
- Calford MB (1983) The parcellation of the medial geniculate body of the cat defined by the auditory response properties of single units. *J Neurosci* 3:2350–2364.
- Calford MB, Aitkin LM (1983) Ascending projections to the medial geniculate body of the cat: evidence for multiple, parallel auditory pathways through the thalamus. *J Neurosci* 3:2365–2380.
- Calford MB, Webster WR (1981) Auditory representation within principal division of cat medial geniculate body: an electrophysiological study. *J Neurophysiol* 45:1013–1028.
- Cetas JS, Price RO, Crowe J, Velenovsky DS, McMullen NT (2003) Dendritic orientation and laminar architecture in the rabbit auditory thalamus. *J Comp Neurol* 458:307–317.
- Cetas JS, Price RO, Velenovsky DS, Crowe JJ, Sinex DG, McMullen NT (2002) Cell types and response properties of neurons in the ventral division of the medial geniculate body of the rabbit. *J Comp Neurol* 445:78–96.
- Cetas JS, Price RO, Velenovsky DS, Sinex DG, McMullen NT (2001) Frequency organization and cellular lamination in the medial geniculate body of the rabbit. *Hear Res* 155:113–123.
- Escabi MA, Read HL (2005) Neural mechanisms for spectral analysis in the auditory midbrain, thalamus, and cortex. *Int Rev Neurobiol* 70:207–252.
- Guillery RW (1966) A study of Golgi preparations from the dorsal lateral geniculate nucleus of the adult cat. *J Comp Neurol* 128:21–50.
- Huang CL, Winer JA (2000) Auditory thalamocortical projections in the cat: laminar and areal patterns of input. *J Comp Neurol* 427:302–331.
- Imig TJ, Morel A (1985) Tonotopic organization in ventral nucleus of medial geniculate body in the cat. *J Neurophysiol* 53:309–340.
- Lee CC, Imaizumi K, Schreiner CE, Winer JA (2004) Concurrent tonotopic processing streams in auditory cortex. *Cereb Cortex* 14:441–451.
- Lee CC, Winer JA (2005) Principles governing auditory forebrain connections. *Cereb Cortex* 15:1804–1814.
- Luppi P-H, Fort P, Jouviet M (1990) Iontophoretic application of unconjugated cholera toxin B subunit (CTb) combined with immunohistochemistry of neurochemical substances: a method for transmitter identification of retrogradely labeled neurons. *Brain Res* 534:209–224.
- Middlebrooks JC, Zook JM (1983) Intrinsic organization of the cat's medial geniculate body identified by projections to binaural response-specific bands in the primary auditory cortex. *J Neurosci* 3:203–225.
- Miller LM, Escabi MA, Read HL, Schreiner CE (2001) Functional convergence of response properties in the auditory thalamocortical system. *Neuron* 32:151–160.
- Morel A, Imig TJ (1987) Thalamic projections to fields A, AI, P, and VP in the cat auditory cortex. *J Comp Neurol* 265:119–144.
- Morel A, Rouiller E, de Ribaupierre Y, de Ribaupierre F (1987) Tonotopic organization in the medial geniculate body (MGB) of lightly anesthetized cats. *Exp Brain Res* 69:24–42.

- Morest DK (1964) The neuronal architecture of the medial geniculate body of the cat. *J Anat (Lond)* 98:611–630.
- Morest DK (1965) The laminar structure of the medial geniculate body of the cat. *J Anat (Lond)* 99:143–160.
- Read HL, Winer JA, Schreiner CE (2001) Modular organization of intrinsic connections associated with spectral tuning in cat auditory cortex. *Proc Natl Acad Sci U S A* 98:8042–8047.
- Read HL, Winer JA, Schreiner CE (2002) Functional architecture of auditory cortex. *Curr Opin Neurobiol* 12:433–440.
- Rodrigues-Dagaëff C, Simm G, de Ribaupierre Y, Villa A, de Ribaupierre F, Rouiller EM (1989) Functional organization of the ventral division of the medial geniculate body of the cat: evidence for a rostro-caudal gradient of response properties and cortical projections. *Hear Res* 39:103–125.
- Rouiller EM, de Ribaupierre F (1985) Origin of afferents to physiologically defined regions of the medial geniculate body of the cat: ventral and dorsal divisions. *Hear Res* 19:97–114.
- Schreiner CE, Read HL, Sutter ML (2000) Modular organization of frequency integration in primary auditory cortex. *Annu Rev Neurosci* 23:501–529.
- Schreiner CE, Sutter ML (1992) Topography of excitatory bandwidth in cat primary auditory cortex: single-neuron versus multiple-neuron recordings. *J Neurophysiol* 68:1487–1502.
- Smith PH, Populin LC (2001) Fundamental differences between the thalamocortical recipient layers of the cat auditory and visual cortices. *J Comp Neurol* 436:508–519.
- Stanton SG, Harrison RV (2000) Projections from the medial geniculate body to primary auditory cortex in neonatally deafened cats. *J Comp Neurol* 426:117–129.
- Winer JA (1985) The medial geniculate body of the cat. *Adv Anat Embryol Cell Biol* 86:1–98.
- Winer JA, Diamond IT, Raczkowski D (1977) Subdivisions of the auditory cortex of the cat: the retrograde transport of horseradish peroxidase to the medial geniculate body and posterior thalamic nuclei. *J Comp Neurol* 176:387–418.
- Winer JA, Kelly JB, Larue DT (1999) Neural architecture of the rat medial geniculate body. *Hear Res* 130:19–41.
- Winer JA, Miller LM, Lee CC, Schreiner CE (2005) Auditory thalamo-cortical transformation: structure and function. *Trends Neurosci* 28:255–263.
- Winer JA, Morest DK (1983a) The medial division of the medial geniculate body of the cat: implications for thalamic organization. *J Neurosci* 3:2629–2651.
- Winer JA, Morest DK (1983b) The neuronal architecture of the dorsal division of the medial geniculate body of the cat. A study with the rapid Golgi method. *J Comp Neurol* 221:1–30.

(Accepted 20 November 2007)
(Available online 28 January 2008)